

Stability analysis of optofluidic transport on solid-core waveguiding structures

Allen H J Yang¹ and David Erickson^{2,3}

¹ School of Chemical and Biomolecular Engineering, Cornell University, Ithaca, NY 14850, USA

² Sibley School of Mechanical and Aerospace Engineering, Cornell University, Ithaca, NY 14850, USA

E-mail: de54@cornell.edu

Received 8 June 2007, in final form 22 October 2007

Published 4 January 2008

Online at stacks.iop.org/Nano/19/045704

Abstract

Optofluidic transport involves the use of electromagnetic energy to transport nanoparticles through the exploitation of scattering, adsorption and gradient (polarization) based forces. This paper presents a new approach to stability analysis for a system of broad applicability to such transport, namely the optical trapping of dielectric particles in the evanescent field of low index (polymer) and high index (silicon) solid-core waveguide structures integrated with microfluidics. Three-dimensional finite element based simulations are used to determine the electromagnetic and hydrodynamic field variables for the system of interest. The net force acting on particles is determined through evaluation of the full Maxwell and flow shear stress tensors, and a trapping stability number is obtained by comparing the work required to remove a particle from the waveguide with available random thermal energy. These forces are correlated to controllable experimental parameters such as particle size, fluid velocity, and channel height, and a series of trapping stability diagrams is produced which detail the conditions under which optofluidic transport is possible.

(Some figures in this article are in colour only in the electronic version)

1. Introduction

Lab-on-a-chip devices are on the verge of becoming self-contained laboratories confined to the size of a computer chip. Incorporating microfluidic and nanofluidic transport networks, these devices have enabled the miniaturization of many of the important unit operations used in large-scale chemical and biochemical processes [1]. The last ten years has seen the development of devices which allow for the mixing [2], separation [3], reaction [4], and detection of chemical and biological species [5], all done with costs and an efficiency not seen in beaker-scale laboratory techniques. Advantages of these techniques include: (1) decreased use of reagents, and hence lower costs, (2) the confinement of processes to small volumes, which decreases the time needed for reactions and sensor detection mechanisms, and (3) the ability to build complex networks, allowing for multiplexed processing.

Key to the development of these devices is the integration of fluidic environments with electrical and optical components.

'Optofluidics' [6] represents a subfield related to the latter of these and involves the exploitation of the unique physics presented by the coupling of nanophotonics with microfluidics and nanofluidics. Numerous devices have demonstrated the ability to actively manipulate optical energy within such systems as a means to generate complex trapping fields [7], sort flowing targets in microfluidic channels [8], and levitate particles through radiation pressure [9]. Prominent amongst these examples, MacDonald *et al* [10] incorporated the use of microfluidic and optical elements to design a size-based real-time particle fractionalization system. Their method relies upon the generation of a periodic optical landscape that is designed to deterministically separate smaller particles from larger ones based on a coupling between the net electromagnetic and hydrodynamic forces imparted on the particles.

Of particular interest to chip based integrated microfluidic systems are solid-core waveguide based devices, which serve to confine light within solid structures through total internal reflection and can interact with small particles via their

³ Author to whom any correspondence should be addressed.

evanescent field. Such systems are designed so that this interaction generates optical scattering/absorption forces for propulsion and gradient (trapping) forces for confinement along the waveguide. The result is an effective ‘optical train track’ for particle transport. A number of experimental works have recently been published which demonstrate various implementations of this effect. Kawata and Sugiura [11], for example, demonstrated the use of an evanescent field based optical trapping technique. Gaugiran *et al* [12] demonstrated the use of silicon nitride waveguides for trapping and propulsion of biological cells. That paper also presents a finite element analysis as a means of predicting the optical forces for a dielectric particle interacting with a waveguide. Other propulsion experiments have used gold nanoparticles [13] and Y-branch waveguides for sorting [14]. Theoretical analyses of waveguide based propulsion have been presented for both Mie regime systems [15] (for particles much larger than the wavelength) and Rayleigh regime systems [16] (where the electromagnetic field around the particle is relatively uniform). Almaas and Brevik [17] and Ng *et al* [18] also both deal specifically with the behavior of particles in evanescent fields.

The aforementioned works presented models for the prediction of propulsive velocities and trapping forces within a static fluidic environment. The greater challenge in developing a practical optofluidic transport system lies in understanding the conditions that bring a particle to a waveguide trap and remain stably trapped within the evanescent field. In this paper, we present a new analytical approach to determining these conditions and examine how they are affected by experimental conditions such as flow speed, nanoparticle diameter and channel height. The three-dimensional numerical modeling of the electromagnetics and hydrodynamics of the system along with the development of a trapping stability parameter enables the development of a series of stability diagrams which detail the regimes in which stable optofluidic transport is possible. In this paper we conduct two case studies, representative of high and low index contrast waveguide systems, and translate our model into important design considerations for future devices.

2. Theory

2.1. Model system and assumptions

Figure 1 illustrates the model system and computational domain used in this study. The model is representative of a waveguide that is clad in a fluid environment. This creates a hybrid system where the evanescent mode exists in the fluid medium, and thus suspended particles can access the mode and interact with the waveguide structure. We specify a flow system where the channel height is constrained, but the length and width are very large relative to the waveguide and system dimensions. This is typical of most microfluidic systems, and can be modeled as laminar flow in the low Reynolds number regime. The perpendicular orientation of the channel and waveguide exploits the orthogonal nature of the propulsion and trapping forces, reducing the trapping problem to one dimension.

Our case studies focus on two different waveguide systems. One case considers a high index contrast system

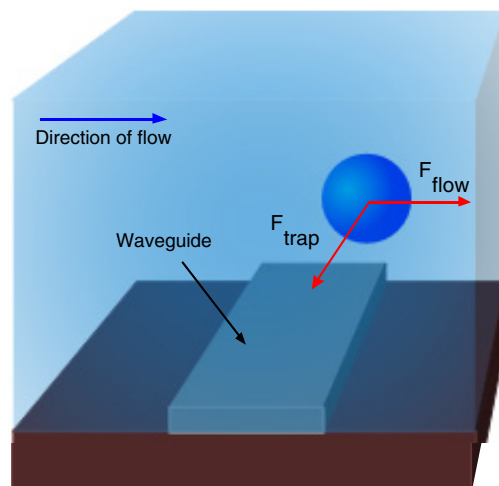


Figure 1. Schematic of modeling system. The microfluidic channel is oriented with flow perpendicular to the waveguide. A particle near the waveguide would then experience a combination of drag forces from fluid flow and trapping forces which emanate from the waveguide.

where the refractive index of the waveguide is much higher than that of the fluid medium. Our basis for this case study is on silicon waveguide systems, which operate at 1550 nm. The low index contrast system is representative of a recent trend in the development of polymer based waveguide systems. The refractive indices of polymers can range from 1.3 to 1.7. The exact value of the refractive index is often dependent upon the particular wavelength coupled into a waveguide. Two polymers commonly used in waveguide fabrication are poly-methylmethacrylate (PMMA) [19] and SU-8 cross-linked polymer [20]. The interested reader is directed to the *Handbook of Optical Materials* [21] for more information regarding polymer refractive indices. We chose a refractive index ($n = 1.68$) to be representative of a polymer with a relatively high refractive index but still exhibiting significantly different stability behavior to that of silicon. Operation at a wavelength of 1064 nm maintains single-mode operation of the polymer waveguide. In both these cases, we assume that optical adsorption by the surrounding liquid medium does not significantly affect the trapping stability.

We also neglect electrical double layer (EDL) repulsion effects [22, 23], which arise as a result of the formation of a surface charge screening layer surrounding both the particle and the waveguide. When a particle approaches the waveguide a repulsion force will exist between the two similarly polarized surfaces. The characteristic length of the decay of the EDL is represented by the Debye length (see the above references). For a solution containing 1 μM ionic strength, the Debye length is approximately 300 nm, which could prevent particles from interacting with the waveguide evanescent field. Higher ionic strengths allow for the shielding of the double layer and reduce the Debye length. At a 100 mM ionic strength the Debye layer is approximately 1 nm thick, and therefore double layer effects can likely be neglected. Furthermore, we do not consider the effect of time-variant changes in the local

refractive index that might arise from a highly concentrated particle suspension, or the trapping of multiple particles.

2.2. Electromagnetics

The time-independent propagating solution for the electromagnetic field can be found using the wave equation for the electric field:

$$\nabla \times \left(\frac{1}{\mu_r} \nabla \times \mathbf{E} \right) - k_0^2 \epsilon_r \mathbf{E} = \mathbf{0} \quad (1)$$

where \mathbf{E} is the electric field, μ_r is the relative permeability, k_0 is the free space wavenumber, and ϵ_r is the relative permittivity. The other field variables can be calculated once the electric field is found. The interactions between an optical field and microscopic dielectric objects are summarized as three types of force. The trapping force, also known as a gradient force, results from the temporary polarization of a dielectric particle in a non-uniform field. The field induces a stronger force on the particle in the direction of higher field intensities, leading to a net movement of the particle in that direction. As the name suggests, the trapping force is the most important aspect of an optical trap. The other two forces combined are responsible for the phenomenon known as radiation pressure, which is the movement of a particle along the direction of optical propagation. The scattering force is described as the momentum transfer associated with the scattering of a photon off the particle, while the absorption force occurs as a result of the adsorption and emission of photons by the particle. Therefore, when a particle is only exposed to a single incident field, assuming no major changes to the field intensity along the propagation direction, movement is a resultant of these two forces. These forces can be described as an electromagnetic stress using the Maxwell stress tensor:

$$\mathbf{T}_M = \mathbf{D}\mathbf{E} + \mathbf{H}\mathbf{B} - \frac{1}{2}(\mathbf{D} \cdot \mathbf{E} + \mathbf{H} \cdot \mathbf{B})\mathbf{I} \quad (2)$$

where \mathbf{T}_M represents the Maxwell stress tensor, \mathbf{E} is the electric field, \mathbf{B} is the magnetic flux field, \mathbf{D} is the electric displacement, \mathbf{H} is the magnetic field, and \mathbf{I} is the isotropic tensor. Since the transport processes of interest here occur on timescales much longer than the optical period, we use the time-independent Maxwell stress tensor $\langle \mathbf{T}_M \rangle$

$$\langle \mathbf{T}_M \rangle = \mathbf{D}\mathbf{E}^* + \mathbf{H}\mathbf{B}^* - \frac{1}{2}(\mathbf{D} \cdot \mathbf{E}^* + \mathbf{H} \cdot \mathbf{B}^*)\mathbf{I} \quad (3)$$

where \mathbf{E}^* and \mathbf{B}^* are the complex conjugates. When expanded out, equation (3) becomes

$$\langle \mathbf{T}_M \rangle = \begin{pmatrix} D_x E_x^* + B_x H_x^* - \frac{1}{2}(\mathbf{D} \cdot \mathbf{E}^* + \mathbf{B} \cdot \mathbf{H}^*) & & & \\ D_y E_x^* + B_y H_x^* & & & \\ D_z E_x^* + B_z H_x^* & & & \\ D_x E_y^* + B_x H_y^* & & & \\ D_y E_y^* + B_y H_y^* - \frac{1}{2}(\mathbf{D} \cdot \mathbf{E}^* + \mathbf{B} \cdot \mathbf{H}^*) & & & \\ D_z E_y^* + B_z H_y^* & & & \\ D_x E_z^* + B_x H_z^* & & & \\ D_y E_z^* + B_y H_z^* & & & \\ D_z E_z^* + B_z H_z^* - \frac{1}{2}(\mathbf{D} \cdot \mathbf{E}^* + \mathbf{B} \cdot \mathbf{H}^*) & & & \end{pmatrix} \quad (4)$$

where the subscripts x , y and z signify the coordinate directions. By integrating the time-independent Maxwell stress

tensor on a surface enclosing the particle of interest, we can determine the total electromagnetic force acting on the system, \mathbf{F}_{EM} , given by

$$\mathbf{F}_{EM} = \oint_S (\langle \mathbf{T}_M \rangle \cdot \mathbf{n}) dS. \quad (5)$$

2.3. Microfluidic transport

Fluid flow is most generally described by the Navier-Stokes equations which contains information about the time-varying convective and diffusive behavior for Newtonian fluids. Liquid flow in a microfluidic system can be assumed to be incompressible and occurring at low Reynolds number. Therefore the simplified set of Stokes flow and continuity equations can be used to model the system. For a system at steady state these equations are

$$\nabla P = \mu \nabla^2 \mathbf{v} \quad (6)$$

$$\nabla \cdot \mathbf{v} = 0 \quad (7)$$

where \mathbf{v} is the velocity, ρ is the density of the fluid, P is the pressure drop in the system, and μ is the viscosity of the fluid. The hydrodynamic force on the particle, \mathbf{F}_H , resulting from fluid flow is described by

$$\mathbf{F}_H = \oint_S (\mathbf{T} \cdot \mathbf{n}) dS \quad (8)$$

where \mathbf{T} is the fluid stress tensor, and n the surface normal vector.

2.4. Trapping stability analysis

In the previous section, we provided a general means of interrogating the electromagnetic force and the drag force on an arbitrary object dependent upon the field variables of the system. Now, consider these forces in the scenario illustrated in figure 2. In this scenario, a particle at some position on the waveguide would experience a net force determined by the vector sum of the two force quantities. It can be shown that the drag force on the particle in our model system is largely unidirectional along the flow axis (we return to validate this assumption in section 3.2). The electromagnetic force from the waveguide acts in two directions, down towards the surface of the waveguide and along the width of the waveguide directing the particle to the nearest local maximum in the evanescent field. In the case of single-mode operation, this maximum would be at the center of the waveguide. Since the trapping force depends on the electric and magnetic field variables, this suggests a relationship between the trapping force and the decay of the evanescent mode. For a planar waveguide the evanescent field can be approximated as

$$E(y, z) = E_0 \exp(-\gamma_e y) \exp(-i\beta_e z) \quad (9)$$

where E is the electric field, γ_e is the extinction coefficient and β_e is the propagation constant (coordinate directions are as given in figure 2). If we assume the spatial force variation

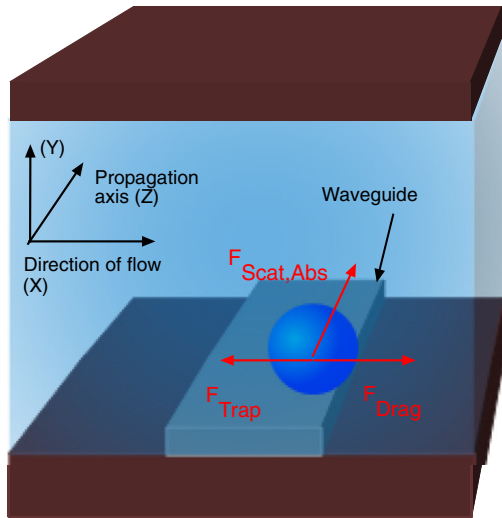


Figure 2. Schematic of relevant optical forces. The particle is assumed to be trapped near the edge of the waveguide. Scattering and absorption forces operate in the direction of optical propagation, perpendicular to the trapping and drag forces.

is like that of the evanescent field, then a similar relationship would hold for a sufficiently wide waveguide:

$$\mathbf{F}_{\text{trap}}(x) = \mathbf{F}_{T0} \exp(-\gamma_f x) \quad (10)$$

where \mathbf{F}_{T0} represents the transverse trapping force at a point $x = 0$, which we designate as the trailing edge of the waveguide, and γ_f is the trapping force decay rate. We will later show numerically that this relationship holds for a particle moving laterally from a rectangular waveguide.

For a constant flow speed, we can assume that the drag forces on the particle are relatively constant compared to the steep decay of the transverse (x -direction) trapping force. Then, the net force acting on the particle is

$$\mathbf{F}_{\text{net}}(x) = \mathbf{F}_{T0} \exp(-\gamma_f x) + \mathbf{F}_D \quad (11)$$

where \mathbf{F}_D is the drag force exerted on the particle. The nature of this equation is such that for any non-zero positive drag force, the net force acting on the particle will at some point become a net positive force (i.e. where the fluidic drag exceeds the trapping force pulling the particle back towards the waveguide). The crossing point can be analytically determined:

$$x_c = \gamma_f^{-1} \ln\left(\frac{\mathbf{F}_{T0}}{\mathbf{F}_D}\right) \quad (12)$$

where x_c is the crossing point where the net force acting on the particle becomes a positive value. The work necessary to release a particle from the trapping field can be shown to be

$$W_{\text{trap}} = \int_0^{x_c} F_{\text{trap}}(x) dx = F_{T0} \gamma_f^{-1} [1 + \theta(\ln(\theta) - 1)] \quad (13)$$

where θ is the ratio of the drag force to the transverse trapping force ($\mathbf{F}_D/\mathbf{F}_{T0}$). The equation is only valid for $0 \leq \theta \leq 1$, and it can be shown that the limit of the nonlinear term goes to unity as θ goes to zero. We can define the trapping stability

Table 1. Simulation parameters.

Object	Material	Domain size ^a	Refractive index
Waveguide (high index)	Silicon	$600 \times 200 \text{ nm}^2$	3.48
Waveguide (low index)	Polymer	$800 \times 400 \text{ nm}^2$	1.68
Substrate	Silicon dioxide	Lower subdomain	1.45
Microfluidic channel	Water	$2 \times 2 \times 5 \text{ } \mu\text{m}^3$	1.33
Particle	Glass	300–600 nm	1.45

^a Waveguide dimensions given as cross section.

of the particle by relating the work needed to release a particle compared to the random thermal motion of the particle, which is important on such size ranges [24]:

$$S = \frac{W_{\text{trap}}}{k_B T} = \frac{F_{T0} \gamma_f^{-1}}{k_B T} [1 + \theta(\ln(\theta) - 1)] \quad (14)$$

where S is the stability number, k_B is the Boltzmann number, and T is the temperature of the system. S can take values greater than or equal to zero, with zero representing a critically unstable trap.

Before continuing it is worthwhile to restate and validate two important assumptions we made in deriving equation (14). The first assumption, from equation (11), was that the drag force does not strongly vary along the x -axis as the particle moves farther away from the waveguide. In an experimental system we expect the drag to change slightly since the distance to the lower wall boundary will change in the transition regime between the particle being over and then off the waveguide. In section 3.3, we will show that this variation tends to be relatively small and that the assumption of constant drag is conservative. The second assumption worth clarifying is from equation (13), where we assume the particle is located such that its x -direction centroid is aligned with the edge of the waveguide. In reality, the true equilibrium position will be set back slightly from the edge to a point where the trapping force and the drag force are equilibrated (the trapping force profile is described in section 3.1). Since this position will vary with particle position and is difficult to predict precisely, we conduct our analysis from the waveguide edge, employing a conservative argument.

2.5. Numerical technique

All numerical solutions are obtained using a commercial finite element package. Our assumptions allow the fluid dynamics and electromagnetic governing equations to be solved separately to reduce the computation time. Using the parameters in table 1, equations (6) and (7) are solved, giving the flow streamlines shown in figure 3. A linear, multigrid solver, with a Vanka algorithm pre-smoother and post-smoother is used to decrease the solution time.

Several rules were followed regarding the geometry of the particle and its relation to the waveguide. The inner sphere represents the physical glass bead, with $n = 1.45$, and it is always positioned with the lowest point 10 nm from the waveguide surface. The outer sphere ($n = 1.33$) is

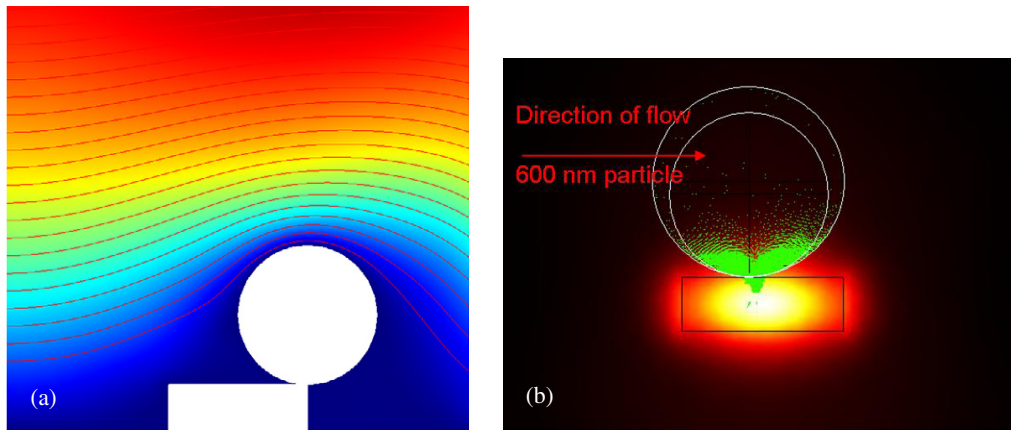


Figure 3. Sample simulation results. (a) Fluid dynamic simulations: cross-sectional image showing flow streamlines and flow velocities (blue represents slower speeds while red represents higher speeds). The particle diameter is 600 nm. The top of the image does not represent the upper boundary of the microfluidic channel. (b) Electromagnetic simulations: cross-sectional image of optical mode profile for silicon waveguide with 600 nm particle. Green arrows depict the direction and magnitude of trapping forces.

the integration region for the Maxwell stress tensor, and it is situated with the lowest point 5 nm from the waveguide surface. The size of the integration sphere was always 120% of the actual glass sphere. This was done to maintain the same size ratio in all simulations.

The boundary conditions for the fluid dynamics simulations are based on common parameters for microfluidic flow in a parallel plate channel. No-slip conditions are used for any physical boundaries in the control volume (the top wall and fluid–solid interfaces). The side boundaries of the simulation volume use a symmetric boundary condition ($\mathbf{n} \cdot \mathbf{u} = 0$ and $\mathbf{t} \cdot \mathbf{u} \neq 0$), $\mathbf{n} \cdot \mathbf{u}$ and $\mathbf{t} \cdot \mathbf{u}$ are the normal and tangential components of the velocity field respectively, which simulate the conditions for Poiseuille flow between two plates. The inlet boundary condition is a fully developed parabolic velocity profile and is defined as $v_x = (3/2)U[1 - (y/H)^2]$, where U is the average fluid velocity, and the channel height is $2H$. The exit boundary condition is a neutral boundary condition ($\mathbf{T} = 0$, where \mathbf{T} is the fluid stress tensor).

For the electromagnetic simulations, the wave equation was solved for the electric and magnetic fields in the waveguide structure and surrounding medium based on the parameters in table 1 using a SPOLES linear direct solver, as seen in figure 3(b). Continuity of the equations is maintained for all internal boundaries, while the surrounding boundaries allow the flux of scattered light, as would be expected in an unbounded fluid medium. The inlet and outlet boundary conditions use the numerical solution from an eigenvalue solver to determine the guided and evanescent mode profiles.

3. Results and discussion

The goal of this paper was to present numerical results detailing the electromagnetic and fluid forces acting on a particle trapped within the evanescent field of a waveguide and to evaluate its trapping stability. In this section, we first compute the trapping force profile along the width of the waveguide while varying its position along the surface.

Next, we look at the exponential decay of the force profile for a particle at positions beyond the waveguide surface, and compare this decay to the extinction rate of the optical field. After determining the initial decay point, where F_0 is evaluated, the fluid and trapping forces are evaluated for different sized particles and fluid velocities to create a diagram of trapping stability based on experimental parameters. Finally, we consider the effect of decreased channel height on the particle drag force and how increased confinement of the particle will lead to a higher likelihood of trapping.

3.1. Near-field trapping force profiles

Here we investigate the near-field transverse and downward trapping forces exerted on a glass particle very near the waveguide surface. Figure 4 illustrates the surface transverse trapping forces for the polymer and silicon waveguide systems, using two different sizes of glass particle. The transverse trapping force is weakest at the center of the waveguide, and strongest towards the edge of the waveguide. Although the particle only has access to evanescent field, directional trapping dependent upon field intensity, even if only along one axis, is still evident. This behavior is commonly associated with free space optical traps where the particle has access to the entire propagating mode. A larger particle for the same waveguide shows stronger trapping, largely due to an increased exposure to the evanescent field.

For the same size particle, the silicon waveguide exhibits stronger surface trapping forces. The much higher refractive index contrast creates a more confined and intense evanescent field, which translates into stronger surface forces. The increased confinement, however, also leads to a faster spatial decay of the evanescent mode. We observe a maximum in the transverse trapping force that occurs near the waveguide edge, which is more pronounced in the case of silicon waveguide. This effect is due to the discontinuous jump in the electric field on the right and left edge of the waveguide, which is necessary for maintaining continuity of the displacement field. As the discontinuity is related to the refractive index contrast, it is not

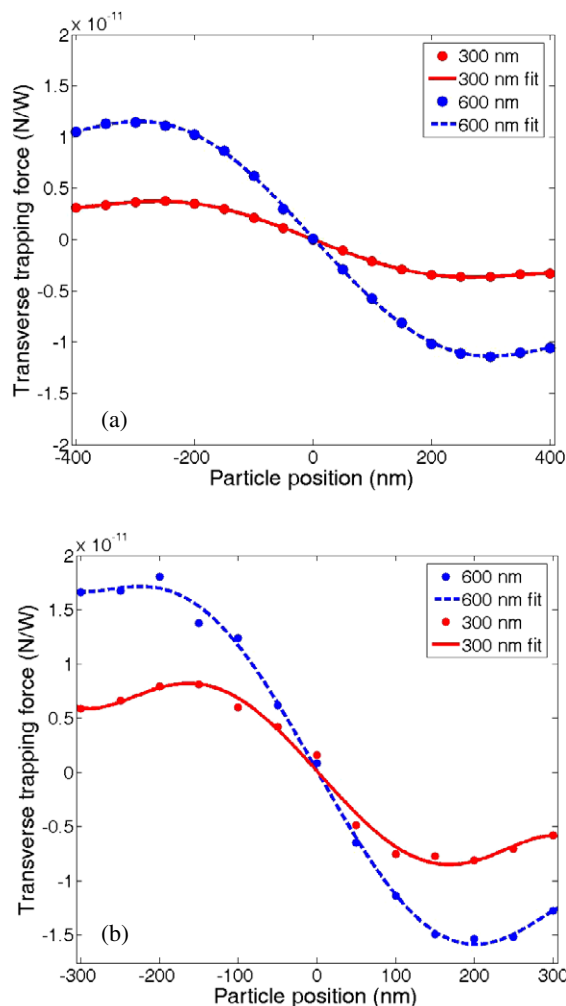


Figure 4. Comparison of transverse trapping force profiles for different waveguide systems. Trapping forces calculated for specified size particles for varying positions along the waveguide surface as illustrated: (a) polymer waveguide, (b) silicon waveguide.

surprising that the increased trapping force near the edge is more significant for the silicon waveguide.

Inherent in our derivations above and additional results outlined below is that the direction in which the trap is most likely to break is in the transverse direction (i.e. parallel to the wall, equivalent to the particle being swept off the waveguide). To support this assumption, figure 5 compares the relative magnitudes of the transverse force pulling the particle towards the center of the waveguide with the Y -axis (figure 2) trapping force acting normal to the main flow direction. As a case study we consider 300 and 600 nm particles on a polymer waveguide. As can be seen at all positions along the waveguide, we found the downward trapping force to be significantly stronger than the transverse trapping force. This was found to be true for all simulated scenarios, independent of particle size and

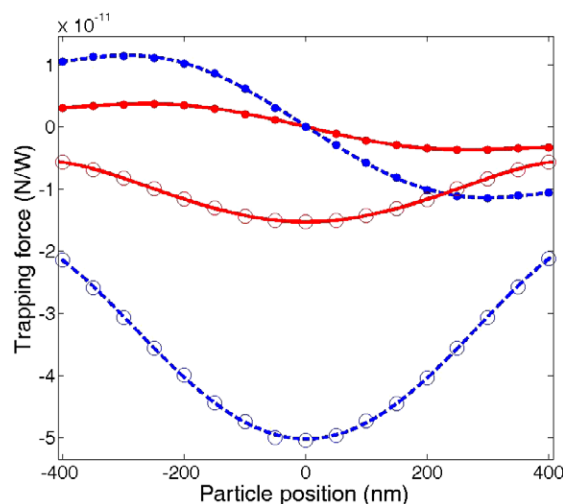


Figure 5. Comparison of downward versus transverse trapping forces for a polymer waveguide. Dashed lines represent 600 nm particles, and solid lines represent 300 nm particles. Filled circles represent transverse trapping forces while open circles represent downward trapping forces.

waveguide type. This suggests that even in the extreme case of a quiescent medium (i.e. no imposed flow) that particle release would be more likely occur from overcoming the transverse as opposed to the downward trapping forces. As such, our assumption is validated.

3.2. Relating simulation variables to experimental parameters

To provide meaningful information in terms of design of an integrated microfluidic waveguide trapping system, it is important to cast the various trapping and drag forces in terms of experimentally relevant parameters. Figure 6 shows the data we obtained from numerical simulations of the trapping and drag forces for spherical glass particles of various sizes fixed at the edge of the waveguide. The Stokes drag law in a free solution predicts a linear relationship with respect to size for a spherical particle in uniform flow. Our simulations predict a power-law relationship with respect to size, while it is linear with respect to the average fluid velocity. As our system is bounded in the z -axis and the flow profile is not uniform, it is not surprising that there is a larger order dependence on the radius of the particle. Figure 6(b) compares the magnitude of the drag force in three orthogonal directions as a function of particle size (transverse = along the direction of flow, parallel = along the direction of the waveguide, lift = along the Y axis normal to the waveguide). As can be seen, the main component of the drag force acts primarily in the transverse direction and the net lift force is significantly weaker for all particle sizes. This, coupled with the results from figure 5, validates our assumption that the most probable path for breaking the trap is in the transverse direction (i.e. the particle being swept off the waveguide along the X axis, as opposed to being lifted off along the Y axis).

As can also be seen in figure 6(a), the trapping forces exhibit a linear relationship for particle sizes ranging from 300 to 600 nm. This arises from the positioning of the particle at

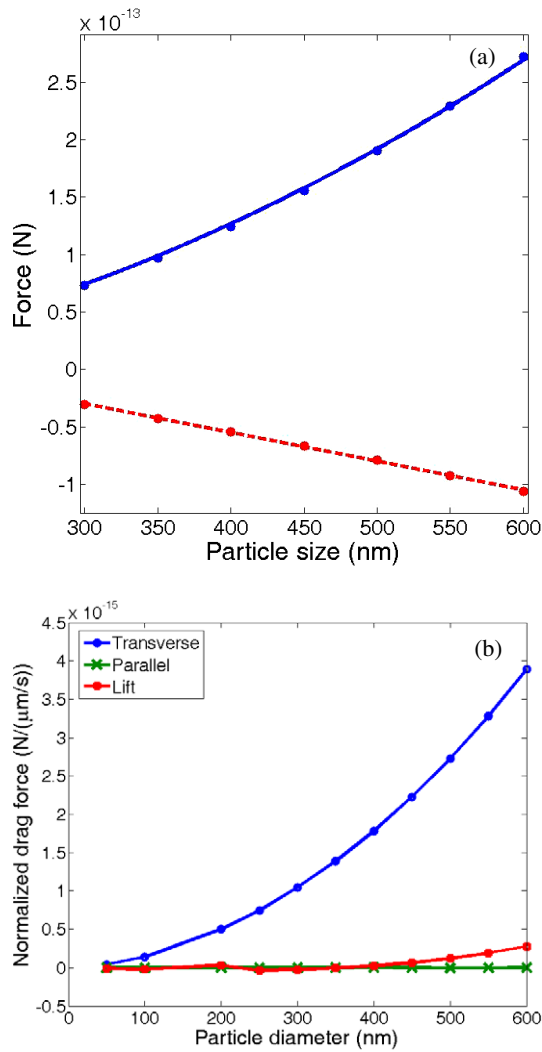


Figure 6. Variation in drag force and initial transverse trapping force (F_{T0} from equation (11)) versus particle size for the case of an average fluid velocity of $80 \mu\text{m s}^{-1}$ and 10 mW of guided optical power in the polymer waveguide. The dashed line represents the transverse optical trapping force while the solid line represents the drag force. Force is presented in absolute quantities at the flow/optical power conditions described above. (b) Correlation of drag forces to particle size. The transverse drag is the same as in (a), the parallel drag is the net drag in the direction along the waveguide, and the lift drag is in the surface normal direction.

the edge of the waveguide, thus allowing large portions of the surface area of the particle to sample lower field intensities (in the region beyond the waveguide edge) relative to areas near the waveguide surface, creating a large gradient in the surface force profile. Our simulations have also shown that the trapping force is linearly dependent upon the coupled power in the waveguide, thus allowing for normalization of our results to reflect this. We expect some type of continuous increasing relationship given that Gaugiran *et al* [12] reported a continuous increasing relationship for propulsion forces versus particle size. Similarly, Ng *et al* [18] derived relationships for the downward trapping force using the Rayleigh approximation which included a size component dependence. However, there are enough deviations in our study that we cannot

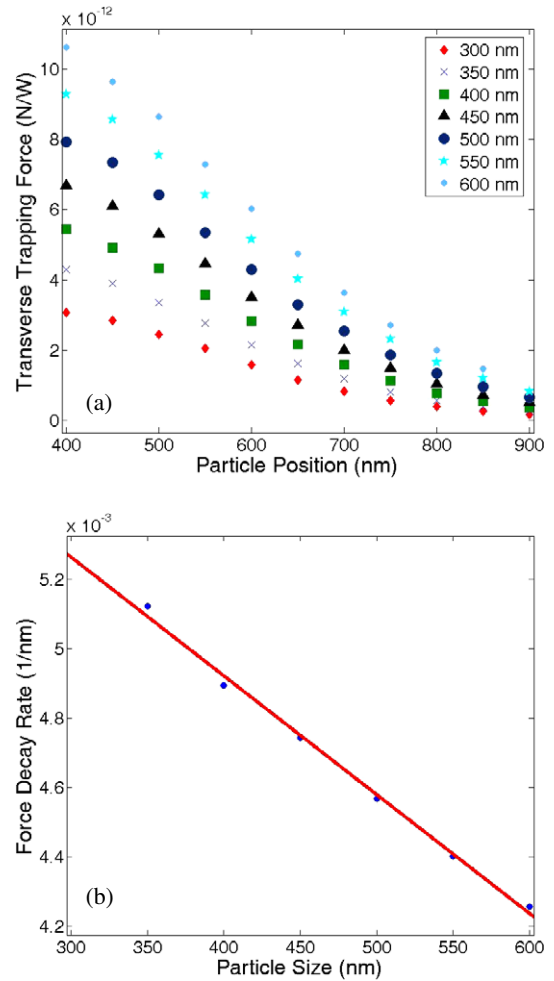


Figure 7. Correlation of trapping force decay rate. (a) Raw data for transverse trapping force beyond waveguide. (b) Linear fit to force decay rate constants as a function of particle size.

quantitatively compare our results with theirs. Our analysis considers the non-uniformity of the evanescent field in the particle volume for larger particle sizes, which is significantly different from a Rayleigh particle analysis.

3.3. Determination of trapping force decay rate (γ_T) and validation of the uniform drag assumption

We previously postulated that the trapping stability of a particle at any given position would be a function of the rate at which the trapping force decays as the particle moves away from the waveguide. Figure 7(a) shows the data obtained for transverse trapping forces for particles at lateral positions beyond the waveguide for particle sizes ranging from 300 to 600 nm. We determine the decay rate by applying an exponential curve fit to the data. Based on this, we correlate the change in the decay rate as a function of particle size. As a reference point, the calculated decay rate for the evanescent field, also known as the extinction coefficient [25], in the polymer waveguide is $6.2 \times 10^{-3} \text{ nm}^{-1}$. The rate for the evanescent field in the silicon waveguide is $8.4 \times 10^{-3} \text{ nm}^{-1}$. Although there is some variance in the decay rate with respect to size, the extinction

coefficient can be calculated without resorting to numerical simulation, and it provides a rough order of magnitude estimate for the force decay rate.

The values for the force decay are of the same order of magnitude as the predicted evanescent decay rate, but differ depending upon the size of the particle in a predictable fashion. Figure 7(b) illustrates the relationship between decay rate and particle size. Similar to the arguments made for the lessened response of the force profile to changes in the evanescent field due to an averaging over large particle surface areas, a similar behavior is observed with slower decay rates predicted for larger sized particles. We expect that as the particle size gets smaller, the force decay rate approaches the extinction coefficient calculated for the evanescent field.

To validate our assumption, described in section 2.4, that the drag force is relatively uniform over the course of the detrapping process we performed a series of simulations to determine the variation in F_D at the first and second multiple of $1/\gamma_t$ (the relevant force extinction length scales in the system). At these distances we found that for the polymer waveguide (for which $1/\gamma_t$ is the largest) the change the drag force decreased by 5% ($1/\gamma_t$) and 13% ($2/\gamma_t$) for the 600 nm particle and less than 1% ($1/\gamma_t$) and 2.5% ($2/\gamma_t$) for the 300 nm particle. As can be seen, the inherent error induced by the assumption is less than 5% over the studied regions. The trap is much stronger in the first multiple of the decay length, and since the drag force decreases, the assumption of constant drag leads to more conservative stability values.

3.4. Trapping stability

Figure 8 illustrates the stability diagram as presented for the polymer and silicon waveguide scenarios. Using the empirical relations we obtained using our data as discussed previously, the independent variables as seen in equation (14) have been correlated to relevant experimental parameters. Based on our equation, the trapping stability number would need to be greater than one for successful trapping to occur. At stability numbers less than one, the trapping is considered to be weaker than the local Brownian motion of the particle; thus successful trapping is highly unlikely. The regions highlighted as 'critically unstable' represent regions where the drag force on the particle is stronger than the calculated trapping force. In such regions, particle trapping should not be possible, unless unrealistically powerful lasers (greater than 100 W) are employed.

In both cases, increases in fluid velocity prove to be detrimental to trapping stability. It is interesting to note that successful particle trapping depends upon maintaining fluid flow below some critical limit, and passing the limit either renders the trapping ineffectual, or enters the critically unstable region. This barrier is significantly lower in the polymer waveguide, largely because the same amount of optical power translates into less trapping force than in a silicon waveguide. This limit can be adjusted, however, by increasing the available power to the waveguide, which would result in a larger region containing a stability number greater than one. Tuning the laser power coupled in the waveguide acts as one means of

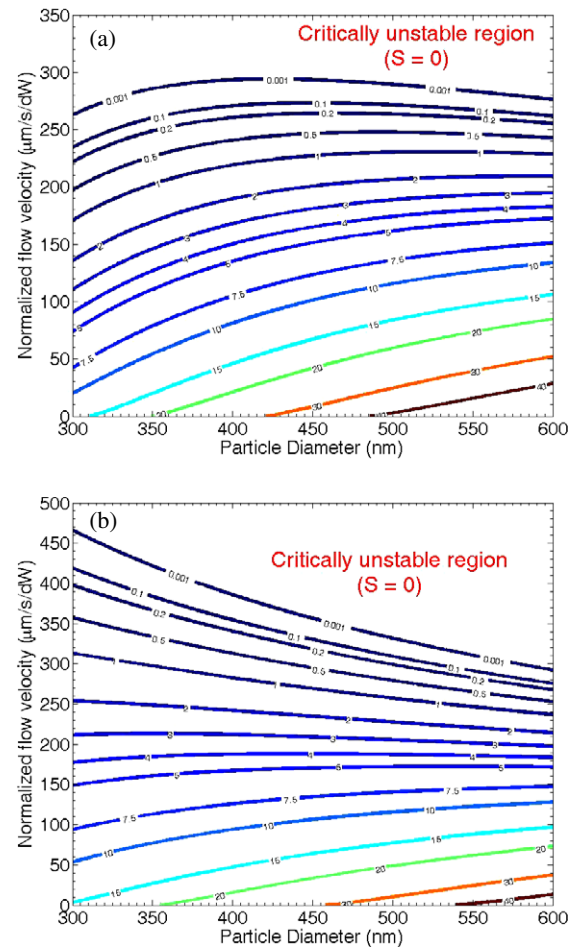


Figure 8. Stability diagrams as a function of experimental parameters. Stability numbers can be calculated for different power ratings (the default is 100 mW) by adjusting the normalized flow rate and stability number by the power ratio (P_{actual} (in mW)/100 mW): (a) polymer waveguide, (b) silicon waveguide.

controllable release, where the trapping forces are reduced by a decrease in the available optical power. Our model system, as specified, provides another method of control, via tuning of fluidic flow rates. Tuning of flow speeds directly alters the drag force on the particle, allowing a non-optical means of adjusting the ability of a particle to overcome the transverse trapping field.

The stability diagram shows distinctly different behaviors between the two waveguide systems when considering different sized particles. We find that the silicon waveguide system demonstrates an improving trend in trapping stability as the particle size gets smaller. Conversely, we find that the polymer waveguide system has a slightly better ability to trap at larger particle sizes. These differences highlight the advantages and disadvantages of a high index versus a low index waveguide system, which we alluded to previously. Although the high index waveguide demonstrates better effectiveness in converting optical power to trapping force, the evanescent field decays over a much shorter distance when compared to a low index waveguide. Thus the optical energy in a high index waveguide is focused into a smaller and stronger trapping field. This would be ideal for holding

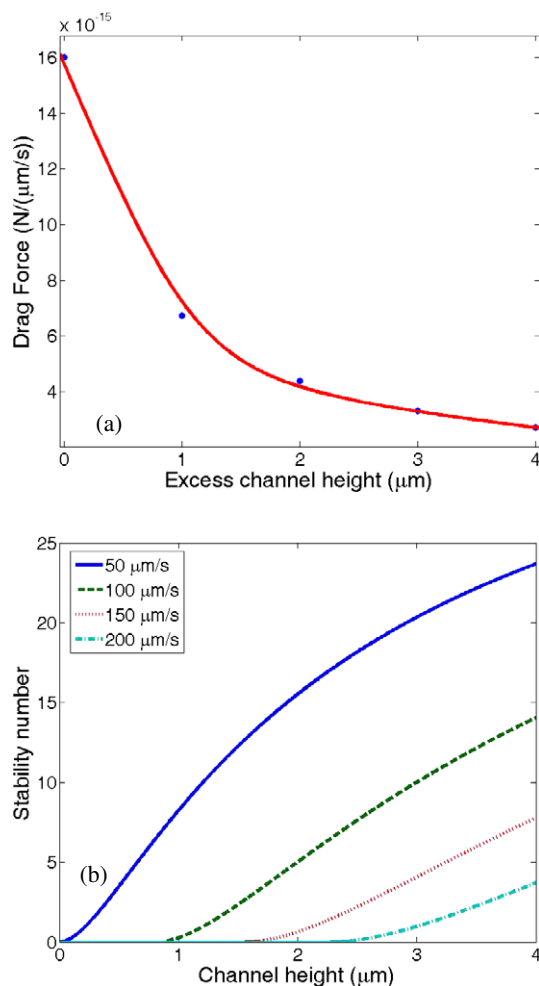


Figure 9. The effect of microfluidic channel height on drag force and stability number. (a) Drag force calculated for a 500 nm diameter particle on a polymer waveguide. The excess channel height is the height in excess of the combined waveguide and particle height. (b) The stability number as calculated for the flow velocities specified for a 500 nm particle with a 100 mW power rating.

smaller particles on the waveguide. The opposite is true for larger particles, which would see a decreasing benefit as the particle size increases beyond the reach of the evanescent field. However, a low index waveguide, while having a lower efficiency, extends the evanescent wave over a longer distance, which would aid trapping of larger particles.

In figure 9, we study the effect of confinement of the microchannel and its influence on the experienced drag force. Due to the nature of our configuration, along the transverse axis, the effective trapping length is solely determined by the width of the waveguide structure, and thus cannot be altered significantly. In the direction of optical propagation, there is no significant change in the trapping and hydrodynamic forces, and the channel width and waveguide length can be considered to be extending indefinitely. Therefore, the only remaining dimension that can be experimentally altered is the microchannel height. Reduction of the channel height decreases the maximum distance a particle can be away from the waveguide when passing the waveguide structure, thus increasing the likelihood that the particle will enter the

evanescent field. This change has a significant impact on the drag force, since the local fluid velocity near the particle will increase as the height decreases, as shown in figure 9(a). Figure 9(b) illustrates the effect of varying channel height for a specific set of parameters. The increase in hydrodynamic force suggests that, for a more confined geometry, the average fluid velocity must be lowered to accommodate the local increases in fluid velocity.

4. Conclusions

In conclusion, we have outlined a comprehensive model for particle trapping stability on waveguide structures integrated with a simple microfluidic channel. Our work highlighted two different classes of optical waveguide, and presented simulations for correlation between trapping forces and experimental parameters. Our results show distinct particle size related advantages over the use of a low index versus a high index waveguide system. The use of optical power and flow speed as control levers by which to aid or detract from particle trapping stability adds another level of control compared to previous experimental devices, and is a step towards the development of a robust trapping system.

In our analysis, we only considered a small range of particle sizes, but chose them such that we could highlight the advantages of such a method where there is no restriction on the uniformity of the electromagnetic field over the particle. The trends we have outlined will allow for better understanding of those experimental systems. This type of analysis could be used in the future for the design of a more sophisticated system incorporating complex photonic elements. Such devices could be used for the complex manipulation of particles in ways that current microfluidics cannot accomplish or for integrated sensing units where trapping, sensing, and release occur at the same location.

Acknowledgments

The authors would like to thank Brad Schmidt and Professor Abraham Stroock for helpful conversations. This work was partially supported by the National Science Foundation under grants CBET-0529045 and CBET-0708599.

References

- [1] Geankoplis C J and Geankoplis C J 2003 *Transport Processes and Separation Process Principles: (Includes Unit Operations)* 4th edn (Upper Saddle River, NJ: Prentice-Hall)
- [2] Stroock A D, Dertinger S K W, Ajdari A, Mezic I, Stone H A and Whitesides G M 2002 Chaotic mixer for microchannels *Science* **295** 647–51
- [3] Song Y A, Hsu S, Stevens A L and Han J Y 2006 Continuous-flow pl-based sorting of proteins and peptides in a microfluidic chip using diffusion potential *Anal. Chem.* **78** 3528–36

- [4] Marcus J S, Anderson W F and Quake S R 2006 Microfluidic single-cell mRNA isolation and analysis *Anal. Chem.* **78** 3084–9
- [5] Zheng G F, Patolsky F, Cui Y, Wang W U and Lieber C M 2005 Multiplexed electrical detection of cancer markers with nanowire sensor arrays *Nat. Biotechnol.* **23** 1294–301
- [6] Psaltis D, Quake S R and Yang C H 2006 Developing optofluidic technology through the fusion of microfluidics and optics *Nature* **442** 381–6
- [7] Chiou P Y, Ohta A T and Wu M C 2005 Massively parallel manipulation of single cells and microparticles using optical images *Nature* **436** 370–2
- [8] Applegate R W *et al* 2006 Microfluidic sorting system based on optical waveguide integration and diode laser bar trapping *Lab Chip* **6** 422–6
- [9] Mandal S and Erickson D 2007 Optofluidic transport in liquid core waveguiding structures *Appl. Phys. Lett.* **90** 184103
- [10] MacDonald M P, Spalding G C and Dholakia K 2003 Microfluidic sorting in an optical lattice *Nature* **426** 421–4
- [11] Kawata S and Sugiura T 1992 Movement of micrometer-sized particles in the evanescent field of a laser-beam *Opt. Lett.* **17** 772–4
- [12] Gaugiran S *et al* 2005 Optical manipulation of microparticles and cells on silicon nitride waveguides *Opt. Express* **13** 6956–63
- [13] Ng L N, Luff B J, Zervas M N and Wilkinson J S 2002 Propulsion of gold nanoparticles on optical waveguides *Opt. Commun.* **208** 117–24
- [14] Grujic K, Helleso O G, Hole J P and Wilkinson J S 2005 Sorting of polystyrene microspheres using a Y-branched optical waveguide *Opt. Express* **13** 1–7
- [15] Jaising H Y and Helleso O G 2005 Radiation forces on a Mie particle in the evanescent field of an optical waveguide *Opt. Commun.* **246** 373–83
- [16] Harada Y and Asakura T 1996 Radiation forces on a dielectric sphere in the Rayleigh scattering regime *Opt. Commun.* **124** 529–41
- [17] Almaas E and Brevik I 1995 Radiation forces on a micrometer-sized sphere in an evanescent field *J. Opt. Soc. Am. B* **12** 2429–38
- [18] Ng L N, Luff B J, Zervas M N and Wilkinson J S 2000 Forces on a Rayleigh particle in the cover region of a planar waveguide *J. Lightwave Technol.* **18** 388–400
- [19] Guo L J, Cheng X and Chao C Y 2002 Fabrication of photonic nanostructures in nonlinear optical polymers *J. Mod. Opt.* **49** 663–73
- [20] Jiang L N and Pau S 2007 Integrated waveguide with a microfluidic channel in spiral geometry for spectroscopic applications *Appl. Phys. Lett.* **90** 111108
- [21] Weber M J 2003 *Handbook of Optical Materials* (Boca Raton, FL: CRC Press)
- [22] Hiemenz P C and Rajagopalan R 1997 *Principles of Colloid and Surface Chemistry* 3rd edn (New York: Dekker)
- [23] Probstein R F 1994 *Physicochemical Hydrodynamics: an Introduction* 2nd edn (New York: Wiley)
- [24] Ashkin A, Dziedzic J M, Bjorkholm J E and Chu S 1986 Observation of a single-beam gradient force optical trap for dielectric particles *Opt. Lett.* **11** 288–90
- [25] Saleh B E A and Teich M C 1991 *Fundamentals of Photonics* (New York: Wiley)